Upper age constraint and paragenesis of the Tiger zone, Rau property, central Yukon

E.J. Thiessen[1], S.A. Gleeson, S.A. Dufrane
Department of Earth and Atmospheric Sciences, University of Alberta

R.C. Carne
ATAC Resources Ltd.

M. Dumala
Archer, Cathro & Associates (1981), Ltd.

Thiessen, E.J., Gleeson, S.A., Dufrane, S.A., Carne, R.C., and Dumala, M., 2012. Upper age constraint and paragenesis of the Tiger zone, Rau property, central Yukon. *In:* Yukon Exploration and Geology 2011, K.E. MacFarlane and P.J. Sack (eds.), Yukon Geological Survey, p. 151-164.

ABSTRACT

The Tiger zone, central Yukon is host to carbonate replacement gold-rich oxide and sulphide mineralization. A paragenetic study has revealed an early mineralization event characterized by hydrothermal dolomites, arsenopyrite and two phases of pyrite, and a late mineralization event that hosts silicate minerals, pyrite, bismuthinite, pyrrhotite and minor base metals and importantly late-stage monazite growth. Two stages of gold mineralization are present and manifest as 1) early arsenopyrite-bearing gold, and 2) a late-stage gold event which is associated with bismuthinite, pyrrhotite, minor base metals and anomalous antimony and arsenic concentrations and are assumed to be related to an adjacent Tertiary intrusive body. A U-Pb age of 58.37 ± 0.93 Ma (2σ) has been obtained from monazites that post-date both gold-bearing phases. The Tiger zone is interpreted to have formed by complex multistage fluid-flow which in part is directly associated with the emplacement and cooling of the 62.9 ± 0.5 Ma Rackla Pluton. Importantly, while the late stage gold-bearing event is the first significant Paleocene intrusion-related gold system identified in Yukon, the age of the earlier gold-bearing event remains unconstrained.

[1] *ericjamesthiessen@gmail.com*

INTRODUCTION

The Tiger zone, Rau property, is located approximately 100 km NE of Mayo (Fig. 1), central Yukon. The deposit is characterized by carbonate-replacement gold-bearing sulphide and oxide mineralization. Sulphide associated gold mineralization reaches 4.04 g/t over 96.01 m in the most well mineralized drill intervals reported (ATAC Resources Ltd., 2009). Only two other carbonate-hosted gold deposits are documented in Yukon, the Osiris showing 100 km east of the Tiger zone and the past-producing Ketza River oxide gold deposit in southeast Yukon (Fig. 1). Several authors have suggested that Ketza River may be an example of a gold-rich, base metal poor manto-type deposit (Fonseca, 1998; Stroshein, 1996), that formed at high temperatures (>300˚C) from hydrothermal fluids derived from intrusive rocks (Kojima *et al.,* 2009; Franchini *et al.,* 2007; Mach and Thompson, 1998). The Osiris deposit, however, is considered analogous to the giant Carlin-type carbonate-hosted disseminated gold deposits (R. Carne, pers. comm., 2011), with the world-class deposits occurring in Nevada, USA. Carlin-type deposits typically feature micron to sub-micron sized gold particles that are associated with disseminated sulphide minerals that occur as stratabound carbonate replacement bodies as well as entirely fault controlled mineralized bodies (Cline *et al.,* 2005; Arehart, 1996). A common model for Carlin mineralization involves derivation of fluids and gold from an igneous source that interacts with meteoric water to dissolve the carbonate host rock and subsequently mineralize the created pore space (*e.g.*, Muntean *et al.,* 2011).

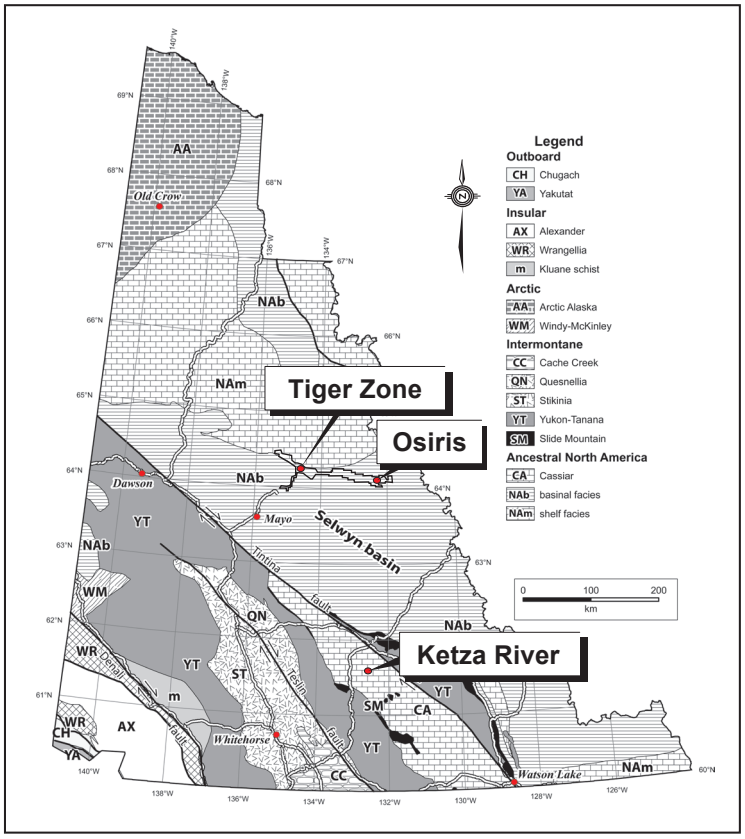

Figure 1. *Terrane map of Yukon illustrating location of the Tiger zone, Osiris and Ketza River occurrence (image courtesy of Yukon Geological Survey).*

Cretaceous age intrusion-related gold systems are common in Yukon and Alaska (Hart, 2007). These gold-bearing systems are often, but not always, characterized by sheeted quartz vein systems that are associated with 1) metaluminous, subalkalic felsic to intermediate intrusions; 2) carbonic hydrothermal fluids; 3) a metal assemblage of Bi, W, As, Mo, Te ± Sb ± Au – base metals; 4) a reduced ore assemblage of arsenopyrite, pyrrhotite and pyrite and a lack of magnetite; 5) aerially restricted and weak hydrothermal alteration; 6) a tectonic setting well inboard of convergent plate boundaries; and 7) within magmatic W and Sn provinces (Lang and Baker, 2001). The best example of reduced intrusion related gold in Yukon is the *ca.* 92 Ma Eagle Gold deposit, located at Dublin Gulch, ~50 km southwest of the Tiger zone (Hart, 2007; Stephens *et al.*, 2004).

The work presented here represents part of a MSc project that will characterize the origin, style, and timing of sulphide-gold mineralization in the Tiger zone in order to establish a deposit model. This paper presents preliminary results regarding the paragenetic history of the Tiger zone, the nature of gold mineralization and some age U-Pb age constraints for Tiger zone mineralization. The mineral paragenesis described herein involved analysis of ~650 core samples from 42 drillholes in addition to petrographic analysis of 95 thin sections from 15 select drillholes.

REGIONAL GEOLOGY

The earliest geological mapping of the Rau property and surrounding areas involved 1:250 000 scale reconnaissance work by the Geological Survey of Canada (Green, 1972; Blusson, 1978). The Tiger zone occurs in a regional Jura-Cretaceous fold and thrust belt comprising rocks of the Selwyn basin and the Mackenzie Platform (Fig. 2) (Abbott *et al.,* 1986). The Selwyn basin is a passive margin succession that accumulated on

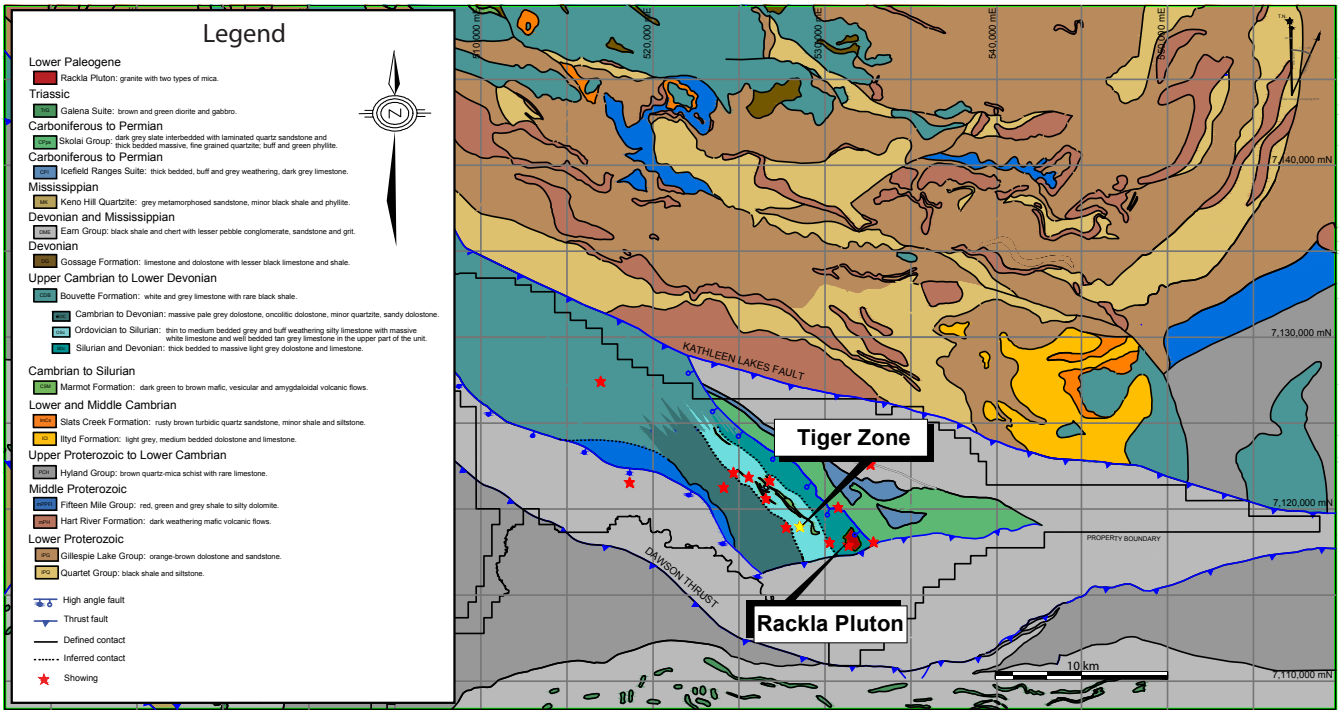

Figure 2. *Regional geology map of the Rau property including the Tiger zone, Rackla Pluton and regional mineral showings (modified from Dumala, 2011, Figure 7-3).*

the western border of ancient North America during the Neoproterozoic to Jurassic. Shallow water platform carbonates of the Mackenzie Platform interfinger with, and bound the time equivalent Selwyn basin rocks to the northeast. Rocks of the Selwyn basin are mostly characterized by deep-water black shales and cherts whereas the Mackenzie Platform is dominated by shelf carbonates (Abbott *et al.,* 1986).

Deformation of these basinal and platformal rocks occurred during the Mesozoic when extensive northeasterly directed compression imbricated and folded the strata (Murphy, 1997). Thrust faults associated with Mesozoic compression are generally oriented north-northeast and northwest (Fig. 2). The Dawson thrust, which broadly separates basinal sedimentary rocks to the southwest (hanging wall) from carbonate platformal rocks to the northeast (footwall; Murphy, 1997), bounds the Rau property on its southern border and occurs ~7 km from the Tiger zone (Fig. 2).

Two suites of intrusive rocks occur within 50 km of the Rau property including the 92 ± 2 Ma Tombstone intrusions and the 64.0-66.8 Ma McQuesten intrusions (Murphy, 1997). Tombstone intrusive rocks range in composition from metaluminous granodiorite to syenite and are well known for their mineral and gold occurrences throughout Yukon (Hart, 2007; Baker and Lang, 2001; Lang and Baker, 2001; Murphy, 1997). McQuesten Suite intrusions comprise peraluminous biotite-muscovite granites and quartz monzonite compositions and have very few associated mineral occurrences (Murphy, 1997). A small granitic stock, the Rackla Pluton intrudes stratigraphy ~3 km east-southeast of the Tiger zone (Fig. 2). A U-Pb zircon age of 62.9 ± 0.5 Ma (2σ) was determined for a large intrusive sill of the Rackle Pluton (V. Bennett, pers. comm., 2010). Additionally, small aplitic and pegmatitic dikes ~1km east of the Tiger zone yielded $^{40}Ar/^{39}Ar$ muscovite ages of 62.3 ± 0.7 Ma, 62.4 ± 1.8 Ma and 59.1 ± 2 Ma (Kingston *et al.*, 2009).

In addition to the Tiger zone, regional exploration on the Rau property has resulted in the discovery of several polymetallic quartz veins ± gold, scheelite-bearing tremolite skarn, pyrrhotite ± scheelite ± chalcopyrite-bearing actinolite-diopside-garnet skarn and wolframite ± tantalite occurrences. Three scheelite-tremolite-actinolite skarn showings occur between the Tiger zone and the Rackla Pluton within the Bouvette Formation (Fig. 2). The most strongly altered skarn occurrences are associated with southwest striking quartz-muscovite-pegmatitic dikes. Geochemical anomalies for these skarns include elevated tungsten, gold and rare copper (Dumala, 2011).

DEPOSIT GEOLOGY

The Tiger zone is hosted by the Bouvette Formation, a carbonate sequence that is broadly assigned to Cambrian to Devonian carbonates of the Mackenzie Platform (Morrow, 1999). These rocks are locally bounded to the south by the Dawson thrust and to the north by the Kathleen Lakes fault (Fig. 2).

The Tiger zone stratigraphy consists of bedded limestones intercalated with locally extensive volcanic flows and volcaniclastic units all of which dip gently to the northeast (Fig. 3). Mineralization is primarily hosted in a carbonate package, the Discovery Horizon, which is bounded to the top (NE) and bottom (SW) by volcanic units (Fig. 3). The intercalated volcanic-carbonate package is truncated to the southwest by a northwest trending high-angle fault (Fig. 3).

Sulphide mineralization also occurs in the Upper Horizon which occurs adjacent to a volcanic unit stratigraphically above the main Discovery Horizon (Fig. 3). East of the Tiger zone, in a carbonate package the stratigraphic equivalent of the Discovery Horizon, is a pyrite-rich gold-poor horizon called the Lower Horizon. The prominent high-angle fault structure that bounds the Tiger zone to the southwest is characterized by a thick sequence of white marble in the immediate footwall and a distinctive volcaniclastic unit informally termed the 'Leopard unit' in the hanging wall (Fig. 3). The Leopard unit is distinctive from other volcanic rocks due to its high calcite content (>50%). Between this unit and the Discovery Horizon, an ~50 cm-thick magnetite bearing white marble typically occurs in sharp contact with the Discovery Horizon and may represent skarn mineralization.

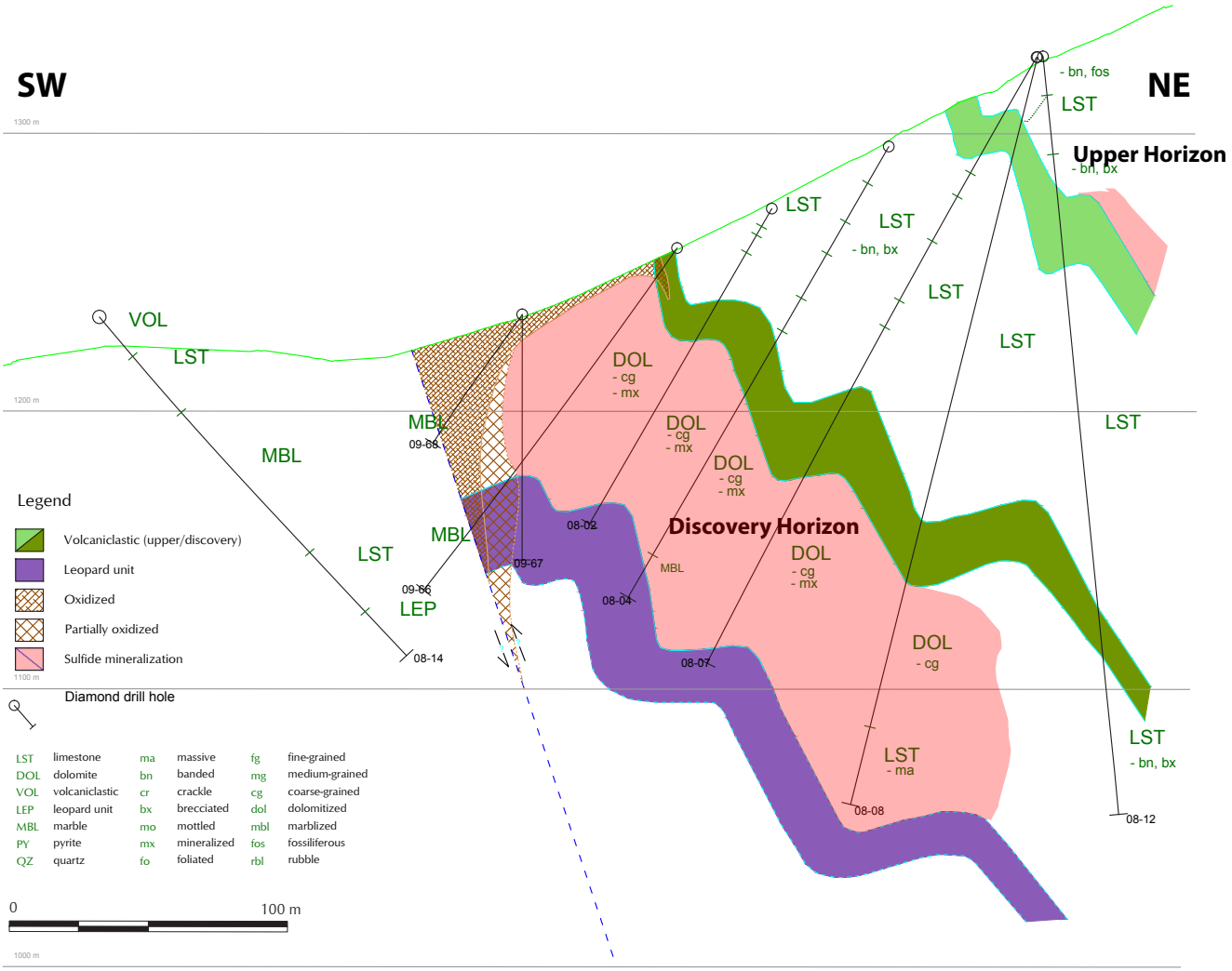

Figure 3. *Generalized cross section of the Tiger zone exemplified by the section line 10+000NW (modified from Dumala, 2011, Figure 11-1). The shaded red zones illustrate the Discovery Horizon and the Upper Horizon sulphide mineralization.*

ANALYTICAL TECHNIQUES

Hand-sample petrographic descriptions and thin section microscopy were supplemented with electron probe micro analyser (EPMA) techniques, including backscattered electron (BSE) imaging and wavelength dispersive spectrometry (WDS), as well as cathodoluminescence (CL) in order to better constrain Tiger zone paragenesis. A Cameca SX100 EPMA was used to analyse trace elements in sulphides, compositional zoning in sulphides and carbonates and for mineral identification by both electron dispersive spectrometry (EDS) and (WDS). Backscattered electron imaging was utilized to image compositional zoning in minerals not apparent by microscopy. A CL microscope was used to identify compositional zoning in carbonates as well as crosscutting carbonate phases not identifiable by microscopy due to epitaxial precipitation. All EPMA analyses were carried out in the Electron Microprobe Laboratory in the Earth and Atmospheric Sciences Department at the University of Alberta.

Laser ablation multicollector inductively coupled plasma mass spectrometry (LA-MC-ICPMS) was also utilized to determine a U-Pb age of monazite identified in the Tiger zone. Age dating was completed at the Radiogenic Isotope Facility in the Department of Earth and Atmospheric Sciences, University of Alberta using a NuPlasma MC-ICPMS and the UP213 laser ablation system by the methods described by Simonetti *et al.,* (2006).

RESULTS – PARAGENETIC SEQUENCE

The paragenesis of the host-rocks and Tiger zone mineralization are summarized in Figure 4 and described below. Four distinct stages of mineralization are documented in the Tiger zone. Stage 1 is host to gold-bearing arsenopyrite + saddle dolomite. Stage 2 comprises pyrite + zoned dolomite. Stage 3 consists of early pyrite + quartz + calcite + talc and late bismuthinite + gold + native bismuth + pyrrhotite associated with anomalous Sb and As suggesting an intrusion-related signature. Lastly, stage 4 hosts quartz + dolomite + sphalerite + minor chalcopyrite + monazite + amphibole + scheelite + muscovite + calcite + pyrite and trace uraninite.

HOST ROCK

Carbonate host rocks of the Bouvette Formation range from lime-mudstones (Fig. 5a) and dolo-mudstones to crinoidal packstones and coral rudstones that commonly have coarse dolomite recrystallization and dolomite replacement textures. These host carbonates are generally devoid of sedimentary structures due to dolomitization

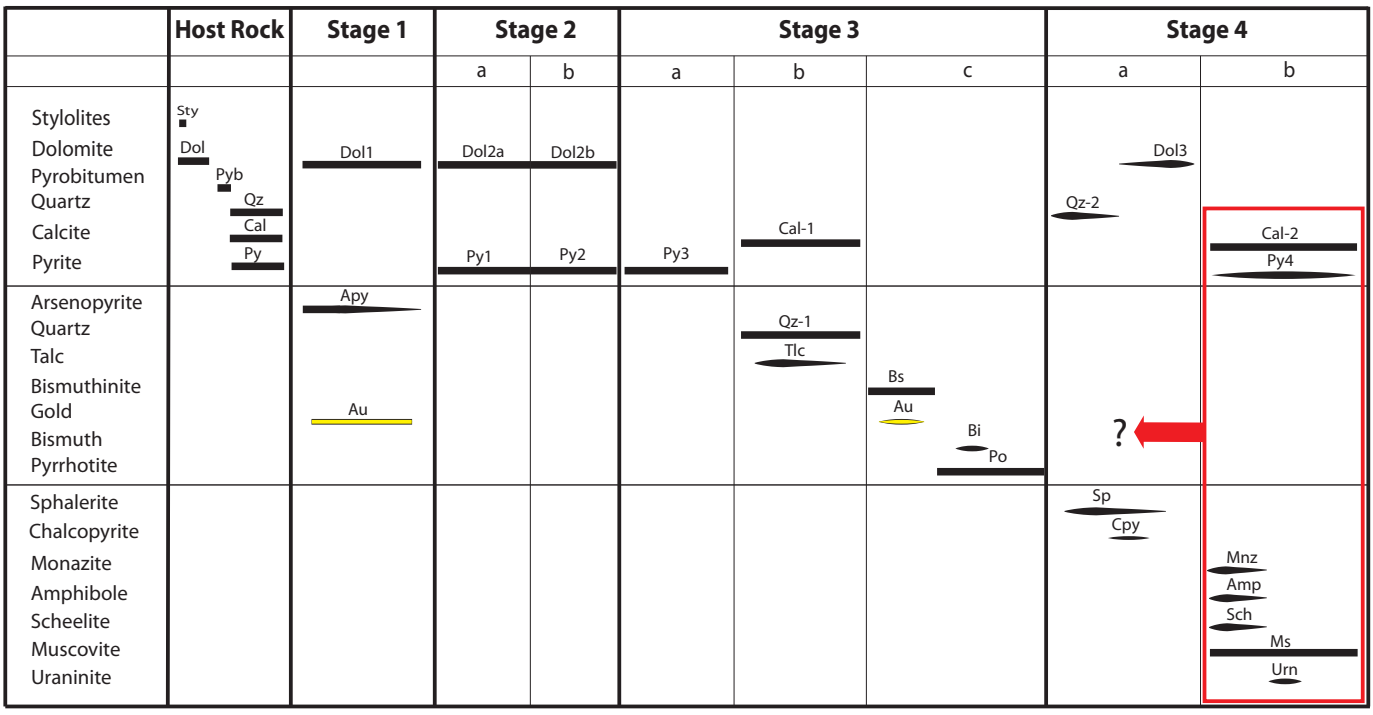

Figure 4. *Paragenesis of the Tiger zone highlighting the two distinct gold-bearing phases. The red box and arrow outlining Stage 4b represents the uncertainty of Stage 4a and 4b as being distinct stages.*

and/or bioturbation. The host carbonates are dark grey in colour and organic material comprises 10-50% of the rock (Fig. 5b). Extensive single-seam stylolite formation sub-parallel with bedding also occurs in these rocks (Fig. 5c).

These carbonates exhibit breccia textures (Fig. 5a,c) throughout the Rau property including brecciation developed within the deposit. The most common breccia type is a mosaic breccia where angular to subangular clasts of carbonate are slightly rotated and separated from one another by up to a few centimetres (Fig. 5c). The breccia fractures exhibit polyphase mineralization beginning with a 'dog tooth' dolomite spar that crystallize on carbonate clasts (Fig. 5a,c). This dolomite spar may form euhedral crystals up to 1 cm long and is commonly rimmed by a thin veneer of sub-millimetre sized tabular pyrobitumen (Fig. 5a,d). The remaining void space is filled by an assemblage of anhedral quartz and calcite with minor anhedral fine-grained pyrite (Fig. 5a).

TIGER ZONE MINERALIZATION

Stage 1: Dolomite 1 + Arsenopyrite + Gold

Stage 1 of the paragenetic sequence involves destructive and pervasive replacement of host-rock carbonate within the Discovery Horizon by dolomite 1 (Dol 1) + arsenopyrite (Apy) + gold (Au). Dolomite 1 (Fig. 5e) occurs as 2-4 mm equant to elongate-feathered and irregular crystals that commonly exhibit saddle morphology (curved crystal faces and sweeping extinction, Fig. 5f). These crystals commonly have angular crystal boundaries shared with other Dol 1 crystals that often exhibit triple-point grain boundaries (Fig. 5f). In hand samples Dol 1 may be a distinctive pale pink colour (Fig. 5e) or white. Both pink and white dolomite have a mottled texture and luminesce dark-red and black under cathodic light (Fig. 6a). This mottled texture is also visible under BSE imaging (Fig. 6b) as light (iron-rich) and dark (magnesium-rich) shades of grey for both pink and white dolomite. The similar chemistries, CL-active species, identical BSE response, and the indistinguishable nature of the pink and white dolomite phases under the microscope indicate a broadly co-eval origin.

Euhedral Apy is disseminated throughout Dol 1 (Fig. 5e). Importantly, Apy grains have angular crystal boundaries and no reaction rim with Dol 1 (Fig. 6c) and, thus, both these phases are considered to be coeval in the paragenetic sequence. Thin, <0.01 mm sub-parallel

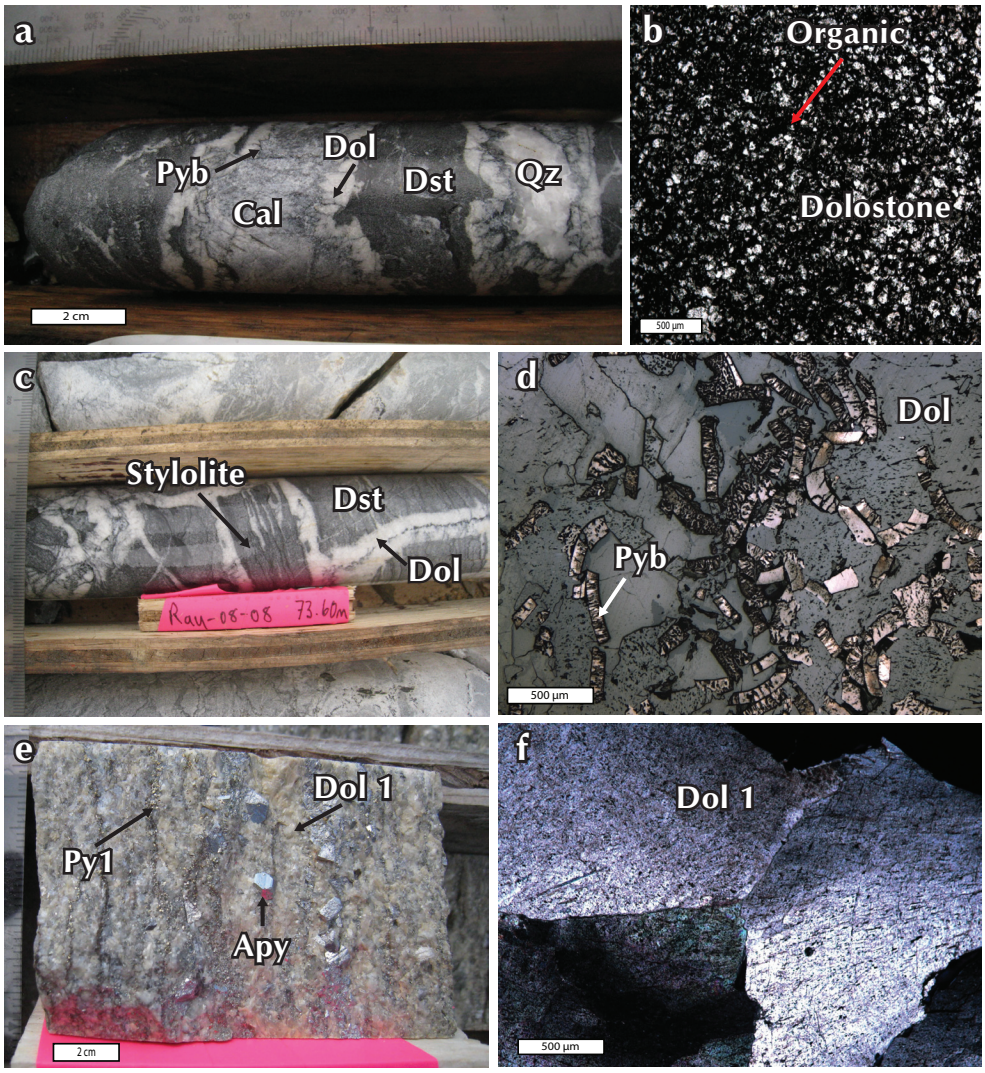

Figure 5. *Paragenesis supporting pictures and images of host-rock and Stage 1 including* ***(a)*** *brecciated host-rock limestone,* ***(b)*** *photomicrograph of organic material within limestone,* ***(c)*** *brecciated limestone clasts exhibiting stylolite development,* ***(d)*** *reflected light picture of pyrobitumen that rims dolomite spar,* ***(e)*** *pale pink Dol 1 with disseminated Apy and foliated Py 1 within the Discovery Horizon sulphide mineralization, and* ***(f)*** *Dol 1 saddle morphology in cross polarized light.*

fractures are restricted to Apy grains but are not observed to extend into the adjacent and inferred coeval Dol 1. Backscattered electron imaging of Apy crystals reveal faint euhedral zoning (Fig. 6c) where the lighter zones are characterized by higher levels of arsenic as quantified by EDS measurements. Eight Apy grain separates have been analysed by solution inductively coupled plasma mass spectrometry. Preliminary results indicate an average gold concentration of 12 ppm in the grains and a maximum value of 19 ppm, suggesting gold mineralization is directly associated with Apy formation.

Stage 2: (a) Pyrite 1+Dolomite 2a, (b) Dolomite 2b+ Pyrite 2

Stage 2a mineralization is characterized by an assemblage of fine-grained pyrite (Py 1) and dolomite (Dol 2a) that have grown in parallel tabular arrays and define a prominent foliation (Fig. 6d). Py 1 occurs as 0.1-0.5 mm equant subhedral-cubic crystals that have grown both interstitially within Dol 1 (Fig. 6e) and overprint Dol 1 and stage 1 Apy (Fig. 6f). Grain boundaries of Py 1 that are in contact with Dol 1 and Apy are sharp (Fig. 6e), have no reaction rimming or dissolution textures (Fig. 6f) and are inferred to be in textural equilibrium with Dol 1 and Apy. These pyrite crystals have a weak preferred orientation and commonly have grain boundary area reduction or triple-point textures (Fig. 7a). Backscattered electron imaging of Py 1 grains reveals that they are broadly homogeneous (Fig. 7b), although weak zoning is rarely observed. Wavelength dispersive spectrometry analysis of the brighter BSE zones of Py 1 grains demonstrates that arsenic-rich portions of crystals have concentrations averaging 2000 ppm As and less commonly containing 1 wt % As.

Dolomite 2a forms 1 mm to 1 cm equant blocky, light grey crystals (Fig. 6d) with angular (Fig. 6b) to irregular crystal boundaries. The abundance of angular crystal faces, absence of both saddle morphology textures and sweeping extinction (under polarized light) and fewer fluid inclusions, distinguishes Dol 2a from Dol 1. Weak undulose extinction and birdseye textures are much more common in Dol 2a. Although no internal deformation or crystal elongation is observed, Dol 2a occurs in elongate mineral clusters sub-parallel to Py 1 (Figs. 6b,d). Angular zonation visible by BSE imaging is characterized by alternating dark and light banding (Fig. 6b). Subsequent EDS analysis of this banding determines that the darker

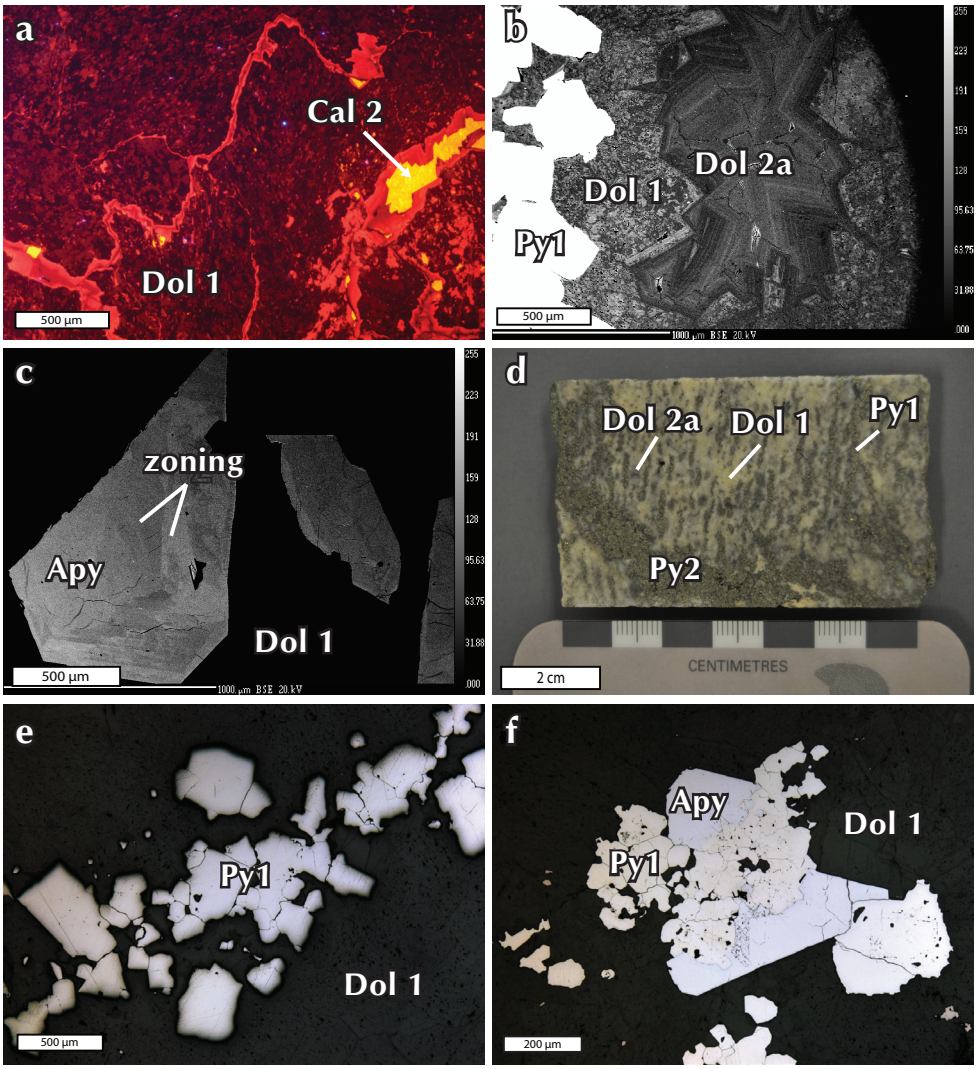

Figure 6. *Paragenesis supporting pictures of Stage 1-2 including* ***(a)*** *cathodic light picture of mottled Dol 1 and interstitial Cal 2,* ***(b)*** *BSE image of Py 1, Dol 1 and Dol 2 displaying mottled Dol 1 and zoned Dol 2a,* ***(c)*** *BSE image of weak zoning in Apy grain,* ***(d)*** *rock sample displaying Py 2 obliquely cross cutting foliated Dol 2a and Py 1 as well as Dol 1,* ***(e)*** *reflected light picture of Py 1 interstitial to Dol 1, and* ***(f)*** *reflected light picture of Py1 crosscutting Apy and Dol 1 in textural equilibrium.*

zones are magnesium-rich and the lighter zones are more iron-rich. Dolomite 2a has a dark-red to black luminescence similar to Dol 1 but is texturally and, we suggest, temporally distinct.

Stage 2b mineralization is characterized by an assemblage of fine-grained pyrite (Py 2) and dolomite (Dol 2b) that post-dates or crosscuts foliation. Py 2 occurs as 0.1-0.5 mm equant subhedral crystals that form irregular crystal masses oblique to Py 1 (Fig. 6d). Py 2 pervasively overprints Stage 1 and Stage 2a mineral assemblages with no preferred orientation (Fig. 6d). Py 2 does not show well-defined zoning in BSE imaging, however, brighter zones also have higher As contents.

Dolomite 2b forms 1 mm to 1 cm equant, blocky, and light grey crystals with angular grain boundaries. This dolomite appears almost identical to Dol 2a, however, Dol 2b does not have a preferred alignment parallel to foliation (Fig. 7c). Backscattered electron imaging of Dol 2a and 2b reveals more uniform growth zoning (Fig. 6b) whereas Dol 1 is characterized by a distinctive mottled appearance with saddle morphology (Figs. 5f, and 6a,b). Electron dispersive spectrometry analysis indicates that darker zones in Dol 2b represent higher Mg concentrations and lighter zones correspond to higher relative Fe contents. Cathodoluminescence colours for zoned Dol 2b range from dark-red to black (Fig. 7d) and are identical to the CL colours and textures of Dol 2a.

Stage 3: (a) Pyrite 3, (b) Quartz 1 + Talc + Calcite 1, (c) Bismuthinite + Gold + Bismuth + Pyrrhotite

Stage 3a mineralization is characterized by coarse-grained, brassy, euhedral to subhedral pyrite (Py 3) that overprints Stage 1 and Stage 2 mineralization. Py 3 is commonly associated with, but pre-dates quartz (Qz 1) (see below), forming crystals in excess of 1 cm in size (Fig. 7e). Backscattered electron imaging shows weak, subangular zoning within the Py 3 phase (Fig. 7f). Brighter BSE zones are determined by WDS to have higher As values, ~1000 ppm.

Stage 3b mineralization consists of variable amounts of Qz 1, talc (Tlc) and calcite (Cal 1) replacing and occurring in brittle fractures crosscutting Py 3 (Fig. 7e) and overprinting Stage 1 and Stage 2 mineral assemblages (Fig. 8a). Quartz 1 is the major constituent of Stage 3b and generally occurs as anhedral accumulations (Fig. 8b) replacing Stages 1 and 2 minerals or more rarely as euhedral crystals. Talc occurs as small 0.1-0.5 mm radiating acicular needles forming fans within Qz 1 (Fig. 8b). The Tlc and Qz 1 share sharp, angular grain boundaries (Fig. 8b) and thus are suggested to be coeval. Calcite 1 is characterized by cm-scale blocky and subhedral crystals

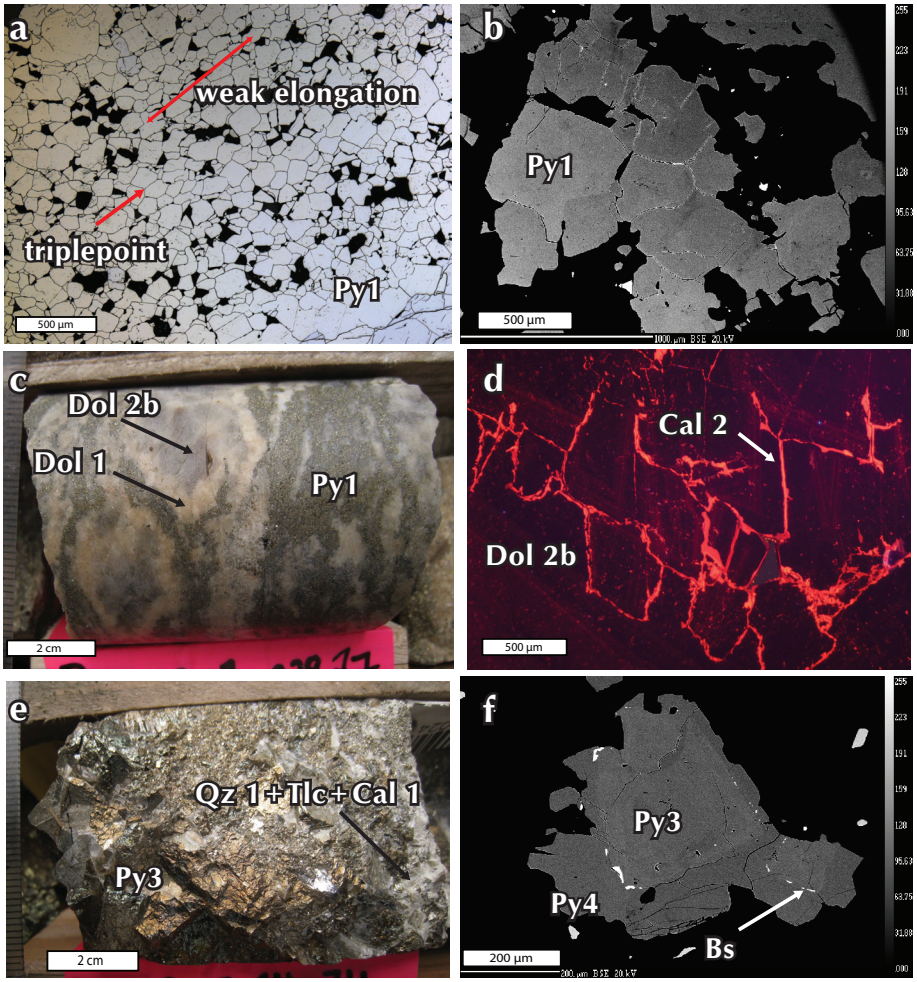

Figure 7. *Paragenesis supporting pictures of Stage 2-3 including* ***(a)*** *reflected light picture of Py 1 displaying elongate grains and triple point textures,* ***(b)*** *BSE image homogenous Py 1,* ***(c)*** *cathodic light picture of zoned Dol 2b and interstitial Cal 2,* ***(d)*** *Dol 2b crosscutting Dol 1 with no preferred orientation,* ***(e)*** *coarse Py 3 and interstitial Qz 1, Tlc and Cal 1, and* ***(f)*** *BSE image of zoned Py 3 rimmed by Bs and subsequent Py 4.*

occurring as a minor phase within quartz (Fig. 8b) or as cm-scale veins crosscutting Py 3.

Stage 3c mineralization consists of bismuthinite (Bs), native gold (Au), native bismuth (Bi) and pyrrhotite (Po) within fractures of Stage 3b Qz 1 and Stage 3a Py 3. Bismuthinite occurs as anhedral crystals within fractures of Stage 1 and Stage 2 sulphides, Py 3 and Qz 1 (Fig. 8c), and has been observed in a few drillholes to occur in large cm-scale accumulations. Backscattered electron imaging has revealed rare bismuthinite rimming Py 3 crystals which in turn are rimmed by a later anhedral pyrite (Fig. 7f). Native gold occurs as anhedral fracture fills within Stage 1 and 2 sulphide fractures and within Py 3 fractures. When native gold is present, it is adjacent to Bs within these fracture fills and suggests coeval growth (Fig. 8d). Analysis of Bs by WDS indicated the grains have elevated Sb (~5000 ppm) and anomalous As (~500 ppm) concentrations. Where observed, native bismuth occurs 'speckled' within Bs as small sub 0.1 mm anhedral crystals and also as fracture coatings of other sulphide phases. Similarly, Po commonly occurs in close proximity to Bs as anhedral masses with no apparent crosscutting relationship. However, native bismuth and Po are observed to crosscut Bs in fractures suggesting a coeval to slightly epigenetic relationship of Po to Bs-Au mineralization.

Stage 4: (a) Quartz 2 + Sphalerite + Chalcopyrite + Dolomite 3, (b) Monazite + Amphibole + Scheelite + Muscovite + Calcite 2 + Pyrite 4 + Uraninite

Stage 4a mineralization is characterized by fracture filling and replacement by quartz (Qz 2), sphalerite (Sp), chalcopyrite (Cpy) and dolomite (Dol 3). This mineral assemblage is commonly observed re-occupying bismuthinite-bismuth veinlets within Py 3 (Fig. 8e). Quartz 2 occurs as small 0.1 mm euhedral crystals along fractures in Py 3 (Figs. 8e,f) which may have Bs rimming the fractures suggesting Qz 2 post-dates Bs growth. These euhedral quartz crystals occur associated with anhedral Sp that also occupy these Py 3 fractures but are also occasionally crosscut by Sp veinlets (Fig. 8f). When Bs and Sp occupy a fracture the Bs is usually rimming the Py 3 crystals whereas the Sp is commonly central to the fracture (Fig. 8e). Rare anhedral crystals of Cpy occur within fractures of Sp (Fig. 9a) suggesting Cpy is coeval to slightly epigenetic to the Sp. In rare, large cm-scale Cal 1 veins, Sp has been observed to occur as mm-scale euhedral zoned crystals that overprint Cal 1. Associated with this phase is a euhedral to anhedral dolomite (Dol 3) that commonly occurs with euhedral Sp and is observed to crosscut and offset fractures filled with Sp.

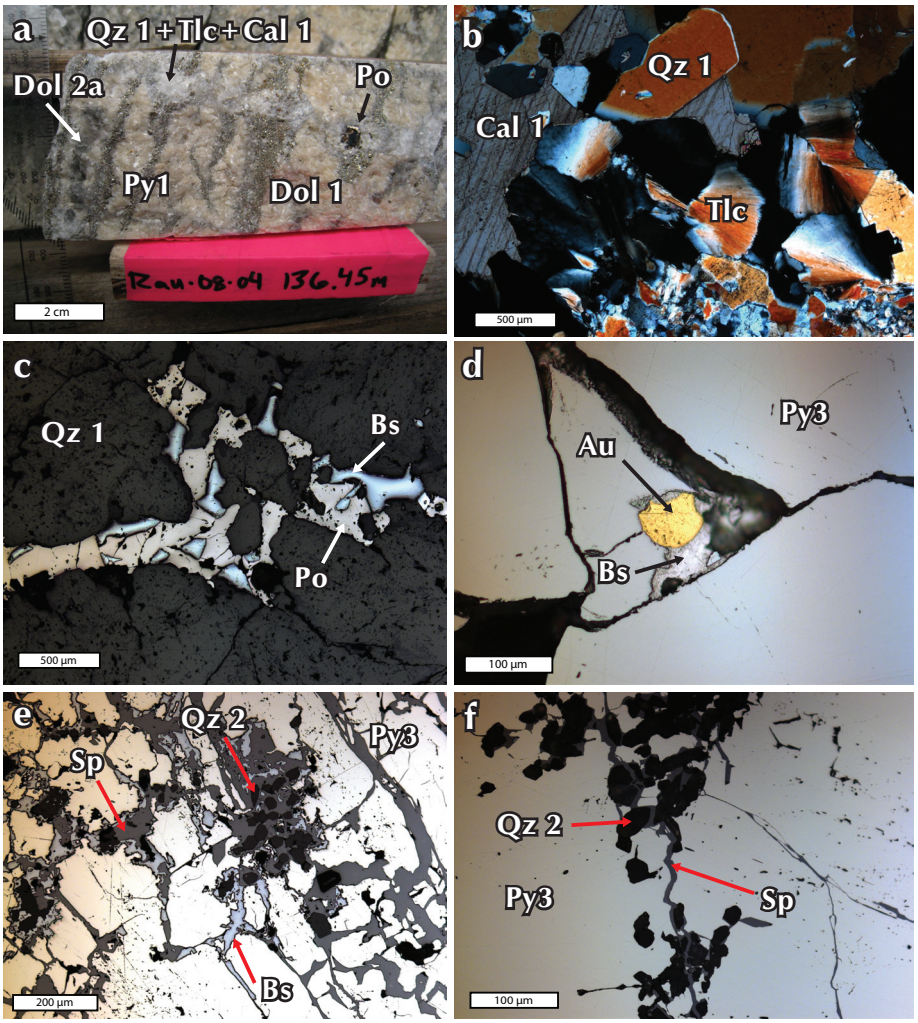

Figure 8. *Paragenesis supporting pictures of Stage 3-4 including* ***(a)*** *Stage 3b minerals crosscutting Stage 1-2,* ***(b)*** *cross polarized light picture of Qz 1, Cal 1 and Tlc in textural equilibrium with each other,* ***(c)*** *reflected light picture of Bs and Po in crosscutting fractures within Qz 1,* ***(d)*** *Au and Bs occurring in fractures of Py 3 in reflected light,* ***(e)*** *reflected light picture of Stage 4a minerals reoccupying Bs veinlets in Py 3, and* ***(f)*** *Sp crosscutting Qz 2 of Stage 4a within Py 3 in reflected light.*

Stage 4b mineralization consists of monazite (Mnz), amphibole (Amp), scheelite (Sch), muscovite (Ms), calcite (Cal 2), uraninite (Urn) and pyrite (Py 4). The main constituent of this phase is Cal 2 and Ms. Cal 2 occurs as subhedral crystals that range from 0.01 mm to 1 cm scale and are intergrown with muscovite (Fig. 9b). Muscovite commonly forms both parallel acicular crystals 0.5 mm long (Fig. 9b) and irregular radiating aggregates. Muscovite and Cal 2 commonly form along rheologic boundaries such as between Dol 1 or 2 and sulphides (Fig. 9c). Pyrite (Py 4) is a minor constituent of this phase and occurs interstitial to the Ms and Cal 2 as small 0.01 mm anhedral crystals (Fig. 9d). Pyrite 4 is also observed rimming earlier Bs (Fig. 7f). Stage 4b mineral phases destructively overprint Stage 1-3 mineral assemblages. Cal 2 has bright red and orange luminescence under cathodic light (Fig. 9b) that are very distinct from Stage 1 (Fig. 9b) and 2 dolomites. Cal 2 also occurs along grain boundaries Dol 1, 2a and 2b determined by CL (Figs. 6a and 7d).

Monazite, Amp and Sch are all present within the Ms-Cal assemblage but are not observed in contact with one another, thus, the relative crosscutting relationships are unclear. Monazite, which is observed to form only within Ms-Cal 2 aggregates, occurs as large 0.5-2 mm euhedral crystals (Fig. 9e). Small fractures in Mnz grains are occupied by Ms or Cal 2 crystals and locally small uraninite grains (Fig. 9e) suggesting monazite pre-dates these minerals. Amphibole is associated with the Ms-Cal 2 assemblage in dense mineral clusters (Fig. 9f). No obvious temporal relationship is observed between Amp grains. Scheelite is an extremely minor component of Stage 4b. It occurs as large 1 cm size subhedral crystals that have fractures infilled with Ms and Cal 2. Stage 4b minerals were not found in association with Stage 4a minerals, and thus the two stages may be coeval.

RESULTS – AGE CONSTRAINTS ON THE TIGER ZONE

The U-Pb age data presented here are the first to constrain a phase of alteration associated with the development of the Tiger zone. The age data represent a minimum (*i.e.*, the youngest possible age the late-stage gold mineralization could be) age of a phase of late-stage gold mineralization.

Earlier attempts to date Tiger zone Apy, Py 1, Py 2, Py 3, Po and Bs by the $^{187}Re/^{187}Os$ method failed due to the low concentrations of ^{187}Re present in those minerals.

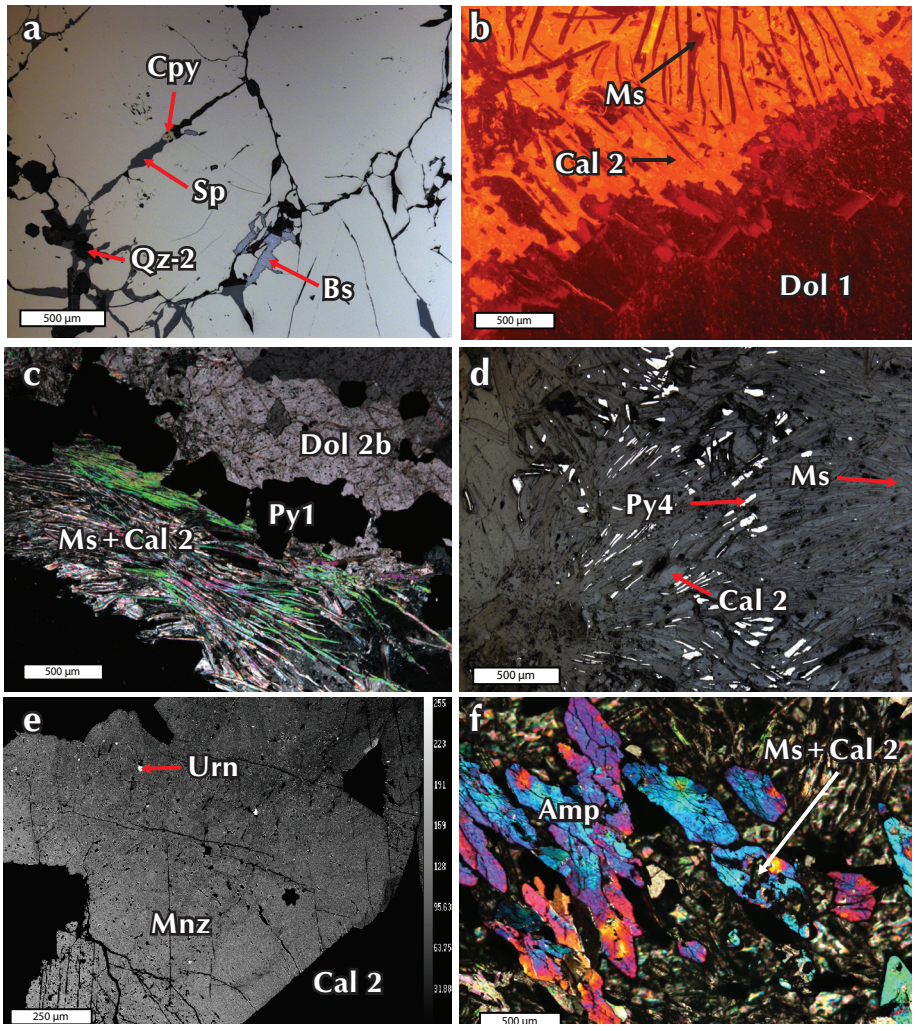

Figure 9. *Paragenesis supporting pictures of Stage 4 including* ***(a)*** *rare Cpy in veinlets of Sp and Qz 2 crosscutting Py 3 in reflected light,* ***(b)*** *cathodic light picture of Ms and Cal 2 overprinting early Dol 1,* ***(c)*** *cross polarized light picture of Ms and Cal 2 precipitating along rheologic boundaries,* ***(d)*** *reflected light picture of Ms, Cal 2 and Py 4 intergrown with each other,* ***(e)*** *BSE image of Mnz where bright spots are uraninite and fractures are filled with Ms, and* ***(f)*** *accumulations of amphibole overprint by Ms and Cal 2 in cross polarized light.*

Four large monazites from Stage 4b were analysed *in situ* by LA-MC-ICPMS (Appendix A). A monazite age of 58.37 ± 0.93 Ma (2σ) was obtained from 38 spots from the four monazites (Figs. 10a,b). High U contents within these monazite grains (up to ~8000 ppm) allowed the resulting precise analytical measurements.

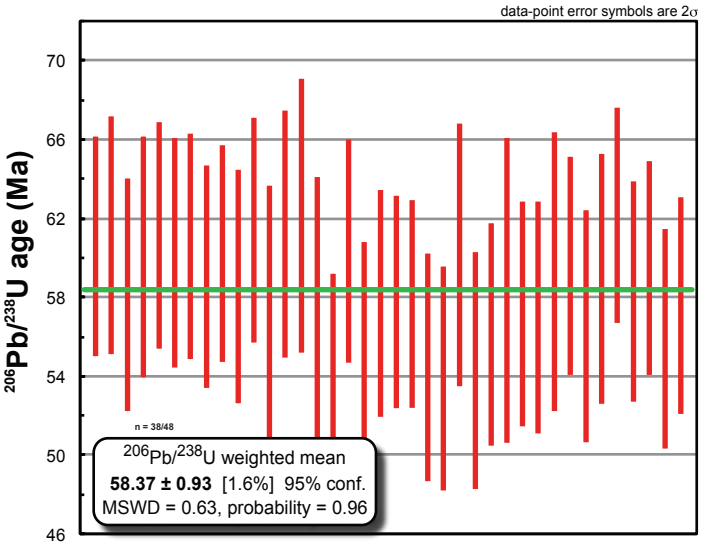

Figure 10. *Plot of weighted mean $^{206}Pb/^{238}U$ ages of 38 spots from 4 monazite grains. Of the 48 total analyses collected, only 38 analyses had reasonable count rates and only these are used to calculate the final weighted mean $^{206}Pb/^{238}U$ ages.*

DISCUSSION

A detailed paragenesis of the Tiger zone reveals two distinct mineralogical assemblages, an early carbonate-sulphide-gold assemblage and a later silicate-sulphide-gold phase.

The first assemblage comprises carbonates, sulphides and gold of Stage 1 and Stage 2. These carbonates pervasively overprint the Discovery Horizon limestone and display abundant coarse-grained, equant, saddle-shaped crystals with triple-point textures and lack significant evidence of veining. Well developed saddle morphology suggests hydrothermal dolomite precipitated in abundant open space. Gold values measured in Stage 1 arsenopyrite grains have concentrations up to 19 ppm Au. This early gold phase does not correlate with high Bi, W, Mo, Te, and Sb concentrations that are typically indicative of an intrusion-related ore-fluid, suggesting that two distinct gold forming events comprise the Tiger zone deposit. Currently, it is unclear whether this early gold is lattice bound to the arsenopyrite or whether the analysed gold was simply free gold from Stage 3c. Further LA-ICPMS analysis will better constrain whether gold is structurally bound in arsenopyrite. The occurrence of Bi, Au, Sb and As (Stage 3c) with minor base metals (Stage 4a) is similar to the element association characteristic of intrusion-related gold deposits. Therefore, late gold in Stage 3c associated with this intrusive signature likely represents a magmatic-hydrothermal event.

Skarn mineralization is commonly associated with intrusion-related systems that intrude into carbonate rocks. Skarn showings that have been identified between the Tiger zone and the Rackla Pluton are predominantly scheelite + amphibole ± gold, an assemblage that resembles Stage 3 and Stage 4 mineral assemblages of the Tiger zone. The uranium-thorium bearing monazite in Stage 4b has also been noted in skarn mineralization (Gross, 1996) and further supports the intrusion-related affinity of Stage 3 and Stage 4 assemblages. Additionally, the magnetite-bearing skarn that occurs basal to the Discovery Horizon crosscuts Stage 1 and Stage 2 mineralization locally and may be related to Stage 3 and Stage 4 mineralization.

The monazite age of 58.37 ± 0.93 Ma (2σ) falls within error of a single $^{40}Ar/^{39}Ar$ muscovite age (59.1 ± 2 Ma 2σ) from nearby granitic aplite and pegmatite dikes but is distinctly younger than two other $^{40}Ar/^{39}Ar$ muscovite ages of 62.3 ± 0.7 Ma and 62.4 ± 1.8 Ma (Kingston *et al.*, 2009). The Rackla Pluton age of 62.9 ± 0.5 Ma (2σ) (V. Bennett pers. comm., 2010) correlates well with the older $^{40}Ar/^{39}Ar$ muscovite ages however, it is at least 3 My older than the mineralization age of the Tiger zone monazite. The age similarities of the pegmatitic dikes and the Rackla Pluton as well as the mineralogical similarities to nearby skarn horizons strongly suggests that the last phase of Tiger zone mineralization is related to the Rackla Pluton.

CONCLUSIONS

Four distinct stages of mineralization are documented in the Tiger zone: 1) gold-bearing arsenopyrite + saddle dolomite of Stage 1; 2) pyrite + zoned dolomite of Stage 2; 3) early pyrite + quartz + calcite + talc and late bismuthinite + gold + native bismuth + pyrrhotite associated with anomalous Sb and As in Stage 3; and 4) quartz + dolomite + sphalerite + minor chalcopyrite + monazite + amphibole + scheelite + muscovite + calcite + pyrite and trace uraninite of Stage 4.

Tiger zone mineralization is, thus, associated with two distinct gold mineralizing events: early gold in Stage 1 of an unknown age and origin; and Stage 3c gold that has an intrusion-related gold signature which suggests Stage 3 mineralization is related to the 62.9±0.5 Ma Rackla Pluton.

ACKNOWLEDGMENTS

Rob Carne of ATAC Resources Ltd. is thanked for the financial and logistical support provided throughout the duration of this project. Matt Dumala and Julia Lane of Archer, Cathro & Associated (1981), Ltd., have contributed tremendous support during sample collection and through insightful geological discussions. Thanks are given to Venessa Bennett for discussions and critical reviews of this manuscript. This ongoing project has also benefited greatly from the financial support of the Yukon Geological Survey and Sarah Gleeson's NSERC Discovery grant.

REFERENCES

Abbott, J.G., Gordey, S. P., and Tempelman-Kluit, D.J., 1986. Setting of stratiform, sediment-hosted lead-zinc deposits in the Yukon and northeastern British Columbia. *In:* Mineral deposits of the northern Cordillera, J.A Morin (ed.), Canadian Institute of Mining and Metallurgy, Special vol. 37, p. 1-18.

Arehart, G.B., 1996. Characteristics and origin of sediment-hosted disseminated gold deposits: a review. Ore Geology Reviews, vol. 11, p. 383-403.

ATAC Resources Ltd., 2009. ATAC Resources Ltd. intersects 5.11 g/t gold over 70.80 metres on its Rau Gold Property. November 3rd, 2009. Retrieved from http://www.atacresources.com/s/NewsReleases.asp. Web. November 2011.

Baker, T. and Lang, J.R., 2001. Fluid inclusion characteristics of intrusion-related gold mineralization, Tombstone-Tungsten magmatic belt, Yukon Territory, Canada. Mineralium Deposita, vol. 36, p. 563-582.

Blusson, S.L., 1978. Regional geological setting of lead-zinc deposits in Selwyn Basin, Yukon. Current Research, Part A, Geological Survey of Canada, Paper 78-1a, p. 77-80.

Cline, J. S., Hofstra, A., Muntean, J.L., Tosdal, R.M., and Hickey, K.A., 2005. Carlin-Type Gold Deposits in Nevada: Critical Geologic Characteristics and Viable Models. Economic Geology 100th Anniversary Volume, p. 451-484.

Dumala, M., 2011. Assessment Report Describing Geophysics, Soil Geochemistry and Diamond Drilling at the Rau Property; prepared for ATAC Resources Ltd. October 20, 2011.

Fonseca, A.L., 1998. Origin of Carbonate Hosted Gold Rich Replacement Deposits and Related Mineralization Styles in the Ketza River Deposit, Yukon Territory. Unpublished MSc thesis, University of British Columbia, British Columbia, Canada.

Franchini, M.B., Barrio, R.E., Pons, M.J., Schalamuk, I.B., Rios, F.J., and Meinert, L., 2007. Fe Skarn, Iron Oxide Cu-Au, and Manto Cu-(Ag) Deposits in the Andes Cordillera of South-west Mendoza Province (34^0-36^0S), Argentina. Exploration and Mining Geology, vol. 16, p. 233-265.

Green, L.C., 1972. Geology of Nash Creek, Larsen and Dawson Map Areas, Yukon Territory. Geological Survey of Canada, Memoir 364, p. 157.

Gross, G.A., 1996. Skarn iron. *In:* Geology of Canadian Mineral Deposit Types, O.R. Eckstrand, W.D. Sinclair, and R.I. Thorpe (eds.), Geological Survey of Canada, no. 8, p. 489-495 (also Geological Society of America, The Geology of North America, v. P-1).

Hart, C.J.R., 2007. Reduced intrusion-related gold systems. *In:* Mineral deposits of Canada: A Synthesis of Major Deposit Types, District Metallogeny, the Evolution of Geological Provinces, and Exploration Methods, Goodfellow, W.D., (ed.), Geological Association of Canada, Mineral Deposits Division, Special Publication No. 5, p. 95-112.

Kingston, S., Mortensen, J., Dumala, M., and Gabites, J., 2009. Ar-Ar Geochronology and Pb Isotopic Constraints on the Origin of the Rau Gold- Rich Carbonate Replacement Deposit, Central Yukon. *In*: Yukon Exploration and Geology 2009, K.E. MacFarlane, L.H. Weston and L.R. Blackburn (eds.), Yukon Geological Survey, p. 213-222.

Kojima, S., Trista-Aguilera, D., and Hayashi, K.I., 2009. Genetic Aspects of the Manto-type Copper Deposits Based on Geochemical Studies of North Chilean Deposits. Resource Geology, vol. 59, issue 1, p. 87-98.

Lang, J.R. and Baker, T., 2001. Intrusion-related gold systems: the present level of understanding. Mineralium Deposita, vol. 36, p. 477-489.

Mach, C.J. and Thompson, T.B., 1998. Geology and Geochemistry of the Kokomo Mining District, Colorado. Economic Geology, vol. 93, p. 617-638.

Morrow, D.W., 1999. Lower Paleozoic stratigraphy of northern Yukon Territory and northwestern District of Mackenzie. Geological Survey of Canada, Bulletin 538, p. 202.

Muntean, J.L., Cline, J.S., Simon, A.C., and Longo, A.A., 2011. Magmatic-hydrothermal origins of Nevada's Carlin-type gold deposits. Nature, vol. 4, p. 122-127.

Murphy, D. C., 1997. Geology of the McQuesten River Region, northern McQuesten and Mayo map areas, Yukon Territory (115P/14, 15, 16; 105M/13, 14). Exploration and Geological Services Division, Yukon, Indian and Northern Affairs Canada, Bulletin 6, 122 p.

Simonetti, A., Heaman, L.M., Chacko, T., and Banerjee, N.R., 2006. In situ petrographic thin section U-Pb dating of zircon, monazite, and titanite using laser ablation-MC-ICP-MS. Journal of Mass Spectrometry, vol. 253, p. 87-97.

Stephens, J.R., Mair, J.L., Oliver, N.H.S., Hart, C.J.R., and Baker, T., 2004. Structural and mechanical controls on intrusion-related deposits of the Tombstone Gold Belt, Yukon, Canada, with comparisons to other vein-hosted ore-deposit types. Journal of Structural Geology, vol. 26, p. 1025-1041.

Stroshein, R., 1996. Geology and Gold Deposits at Ketza River, Yukon Territory A progress report. *In:* Yukon Exploration and Geology 1995, Exploration and Geological Services Division, Yukon, Indian and Northern Affairs Canada, p. 43-48.

Appendix A. *Selected U-Pb analyses of four monazite grains from the Tiger zone.*

sample name	$^{238}U/^{206}Pb$	2 s	$^{207}Pb/^{206}Pb$	2 σ	$^{206}Pb^*/^{238}U$ age (Ma)	2 σ error (Ma)
MNZ-1F	105.956	9.799	0.046	0.001	61	6
MNZ-1G	104.962	10.374	0.048	0.001	61	6
MNZ-1H	110.449	11.271	0.045	0.001	58	6
MNZ-1I	106.878	10.895	0.046	0.001	60	6
MNZ-1J	104.952	9.907	0.046	0.001	61	6
MNZ-1Q	106.492	10.334	0.046	0.001	60	6
MNZ-1R	105.951	10.025	0.045	0.001	61	6
MNZ-1S	108.693	10.487	0.045	0.001	59	6
MNZ-1T	106.553	9.784	0.045	0.002	60	6
MNZ-1U	109.619	11.133	0.043	0.002	59	6
MNZ-1V	104.520	9.726	0.042	0.001	61	6
MNZ-1W	112.520	13.176	0.040	0.002	57	7
MNZ-2A	104.875	10.772	0.045	0.001	61	6
MNZ-2B	103.280	11.578	0.044	0.002	62	7
MNZ-2C	111.870	13.121	0.043	0.001	57	7
MNZ-2D	119.441	12.196	0.044	0.002	54	5
MNZ-2E	106.321	10.037	0.044	0.001	60	6
MNZ-2F	115.292	10.711	0.044	0.001	56	5
MNZ-2G	111.260	11.138	0.041	0.002	58	6
MNZ-2H	111.116	10.430	0.041	0.003	58	5
MNZ-2I	111.324	10.202	0.043	0.001	58	5
MNZ-2J	117.935	12.526	0.042	0.002	54	6
MNZ-3B	119.169	12.662	0.045	0.001	54	6
MNZ-3C	106.677	11.872	0.045	0.001	60	7
MNZ-3D	118.269	13.198	0.045	0.001	54	6
MNZ-3E	114.405	11.601	0.044	0.003	56	6
MNZ-3F	109.998	14.661	0.046	0.001	58	8
MNZ-3H	112.281	11.260	0.044	0.002	57	6
MNZ-4A	112.621	11.705	0.046	0.001	57	6
MNZ-4B	108.265	12.962	0.045	0.001	59	7
MNZ-4C	107.682	10.095	0.046	0.001	60	6
MNZ-4D	113.553	11.859	0.046	0.001	57	6
MNZ-4E	108.946	11.784	0.046	0.001	59	6
MNZ-4F	103.220	9.117	0.048	0.001	62	5
MNZ-4G	110.075	10.616	0.046	0.001	58	6
MNZ-4H	107.921	9.877	0.046	0.001	59	5
MNZ-4I	114.861	11.485	0.046	0.001	56	6
MNZ-4J	111.489	10.685	0.046	0.001	58	5

not common Pb corrected